

The influence of layering and barometric pumping on firn air transport in a 2D model

Benjamin Birner¹, Christo Buizert², Till J.W. Wagner³, and Jeffrey P. Severinghaus¹

¹Scripps Institution of Oceanography, University of California San Diego, La Jolla, CA 92093, USA

²College of Earth, Ocean and Atmospheric Sciences, Oregon State University, Corvallis, OR 97331, USA

³Department of Physics and Physical Oceanography, University of North Carolina at Wilmington, NC 28401, USA

Correspondence: Benjamin Birner (bbirner@ucsd.edu)

Abstract. Ancient air trapped in ice core bubbles has been paramount to developing our understanding of past climate and atmospheric composition. Before air bubbles become isolated in ice, the atmospheric signal is altered in the firn column by transport processes such as advection and diffusion. However, the influence of low permeability layers and barometric pumping (driven by surface pressure variability) on firn air transport is not well understood and cannot be captured in conventional 1-dimensional firn air models. Here we present a 2-dimensional (2D) trace gas advection-diffusion-dispersion model that accounts for discontinuous horizontal layers of reduced permeability. We find that layering or barometric pumping individually yield too small a reduction in gravitational settling to match observations. In contrast, when both effects are active, the model's gravitational fractionation is suppressed as observed. Layering focuses airflows in certain regions in the 2D model which acts to amplify the dispersive mixing resulting from barometric pumping. Hence, the representation of both factors is needed to obtain a realistic emergence of the lock-in zone. In contrast to expectations, we find that the addition of barometric pumping in the layered 2D model does not substantially change the differential kinetic fractionation of fast and slow diffusing trace gases. However, like 1D models, the 2D model substantially underestimates the amount of differential kinetic fractionation seen in actual observations, suggesting that further subgrid-scale processes may be missing in the current generation of firn air transport models. In spite of this deficiency, we find robust scaling relationships between kinetic isotope fractionation of different noble gas isotope and elemental ratios. These relationships may be used to correct for kinetic fractionation in future high precision ice core studies and can amount to a bias of up to 0.45 °C in noble gas based mean ocean temperature reconstructions at WAIS Divide, Antarctica.

Copyright statement.

1 Introduction

In the upper 50-130 m of consolidated snow above an ice sheet, known as the firn layer, atmospheric gases gradually become entrapped in occluded pores and are eventually preserved as bubbles in the ice below. Antarctic ice core records containing these trapped gases have been critical in informing our understanding of the interplay of past climate and atmospheric trace gas variability over the past 800,000 years (Petit et al., 1999; Lüthi et al., 2008). As atmospheric gases migrate through the firn, they are modified in elemental composition and isotopic signatures by several competing physical processes (Schwander et al., 1988, 1993; Trudinger et al., 1997; Buizert et al., 2012; Kawamura et al., 2013; Mitchell et al., 2015). Therefore, appropriate corrections must be applied to firn and ice core records to accurately reconstruct atmospheric trace gas histories.

Firn is a layered medium, in which the denser layers can impede vertical diffusion and transport (Hörhold et al., 2012; Mitchell et al., 2015; Orsi et al., 2015) (Fig. 1). The significance of these layers for firn gas transport remains unclear and motivates this work. Readers who are familiar with the structure of firn and its air transport processes may wish to skip ahead to the last paragraph of this section. To build some intuition about firn transport processes, a simple analytical model of firn air transport is provided in Appendix A.

Box 1 Porous media terminology

Porosity: the fraction of (firn) volume filled by gas

Permeability: the degree to which a porous medium permits viscous flow to pass through

Fickian diffusion: molecular diffusion that is proportional to the concentration gradient as described by Fick's first law

Tortuosity: measure of the twistedness of pathways through a porous medium

We distinguish four main processes affecting the composition of air in firn: diffusion, advection, dispersion and convective mixing. Molecular diffusion, driven by concentration gradients in the firn, is the primary mode of horizontal and vertical transport. Molecular diffusion also enables gravitational fractionation, or “settling”, of trace gases in proportion to their masses (Schwander, 1989; Sowers et al., 1989; Schwander et al., 1993; Trudinger et al., 1997). Gravitational settling leads to an enrichment of heavy isotopes with depth that is described in equilibrium by the barometric equation (Schwander, 1989; Sowers et al., 1989; Craig et al., 1988):

$$\delta_{grav} = \left[\exp\left(\frac{g\Delta m}{RT}z\right) - 1 \right] \times 1000 \text{ ‰}, \quad (1)$$

where $\delta \equiv \frac{r_{sample}}{r_{standard}} - 1 \equiv q - 1$, with r being the isotope ratio (unitless), z the depth (m), T the absolute temperature (K), Δm the isotope mass difference (kg mol^{-1}), g the gravitational acceleration (m s^{-2}), and R the fundamental gas constant ($\text{J mol}^{-1} \text{K}^{-1}$).

Gradual accumulation of snow and air bubble trapping leads to a slow, downward advection of the enclosed air. The net air advection velocity is slower than the snow accumulation rate (yet still downward in the horizontal average in an Eulerian framework) because compression of the porous firn medium produces a flow of air upward relative to the firn matrix (Rommelaere et al., 1997).

Buoyancy-driven convection and brief pressure anomalies associated with wind blowing over an irregular topography cause strong mixing between the near-surface firn and the unfractionated atmosphere, smoothing concentration gradients (Colbeck, 1989; Severinghaus et al., 2010; Kawamura et al., 2013). This mixing causes substantial deviations from the gravitational settling equilibrium (i.e., the solution to Eq. (1)) and leads to varying degrees of kinetic isotope fractionation because faster
5 diffusing isotopes more readily return to thermal-gravitational equilibrium by diffusion (Buizert et al., 2012; Kawamura et al., 2013).

Lastly, surface barometric pressure variability on longer timescales (>1 hour) drives air movement down to the firn-ice transition. Building on work by Schwander et al. (1988), Buizert and Severinghaus (2016) suggest that surface pressure variability may produce significant pressure gradients in the firn that induce airflow. Porous firn has a high tortuosity, i.e., two points
10 are typically connected by strongly curved paths, and the deep firn also contains many cul-de-sacs (Buizert and Severinghaus, 2016), their Fig. 2). Airflow through such a medium produces mass-independent, dispersive mixing. Dispersion in this context is an emergent macroscopic phenomenon that describes microscopic velocity deviations from Darcy's law of bulk fluid flow in different pores. This process may be accounted for by adding a dispersive mixing term to the advection-diffusion equation traditionally used for trace gas transport in firn (e.g., Buizert and Severinghaus, 2016).

15 Together, these four processes yield a firn column that is split into a surface mixed zone (SMZ, which has historically been labelled the convective zone), a diffusive zone (DZ) and a lock-in zone (LIZ) (Fig. 2). The close-off depth (COD) occurs where the air content becomes fixed and pressure in open porosity increases above hydrostatic pressure. We prefer the term "surface mixed zone" over the more commonly used terminology "convective zone" to acknowledge the dual nature of mixing driven by convection and high-frequency pressure variability in this region. The SMZ is rather well-mixed with a trace gas
20 composition similar to the atmosphere. Nevertheless, large seasonal thermal gradients can lead to isotopic fractionation which is only partially attenuated (Severinghaus et al., 2001, 2010; Kawamura et al., 2013). Molecular diffusion dominates in the DZ but effective firn diffusivity decreases with depth due to the increasing influence of tortuosity hindering diffusion. Throughout the DZ, gravitational settling leads to an enrichment of all isotopes heavier than air in proportion to their mass difference. The top of the LIZ, the somewhat poorly defined lock-in depth (LID) horizon, is commonly deduced from a rather sudden change
25 in the slope of the $\delta^{15}\text{N}$, CO_2 or CH_4 profiles. Gravitational enrichment of isotopes ceases in the LIZ and isotope ratios remain constant with depth. We term any such deviation from gravitational equilibrium "disequilibrium" (without implying that such a situation is not in steady-state).

The physical mechanism responsible for the cessation of gravitational enrichment in the deep firn is still not fully understood. Since CFCs and other anthropogenic tracers have been detected in firn air measurements from the LIZ well below the depth
30 expected from pure advection, it is clear that some amount of vertical transport by molecular diffusion or dispersion continues in the LIZ (Severinghaus et al., 2010; Buizert et al., 2012; Buizert and Severinghaus, 2016). However, no further gravitational settling of isotopes occurs in the LIZ as indicated by constant $\delta^{15}\text{N}$ values. Furthermore, the vertical transport in the LIZ appears to be at least to some degree mass- and diffusivity-dependent since the faster diffusing CH_4 advances further in the LIZ than the slower diffusing gases CFC-113 or CO_2 (Buizert et al., 2012). Therefore, transport in the LIZ cannot be explained
35 by either mass-indiscriminate dispersive mixing or molecular diffusion alone. Most current 1D firn air models use a greatly

reduced molecular diffusivity in the lock-in zone and simultaneously introduce a mass-independent mixing term tuned to match measured trace gas profiles (Buizert et al., 2012). A physical mechanism to justify these numerical methods remains elusive. An attempt at a physical explanation was given by Buizert and Severinghaus (2016), who introduced barometric pumping in a 1D firn model.

- 5 Here, we explore the possibility that non-fractionating trace gas mixing in deep firn may be explained by the combination of barometric pumping and discontinuous horizontal layers that have nominal diffusivity. High density layers are empirically linked to low vertical permeability (and thus diffusivity), increasing the firn’s tortuosity and forcing extensive horizontal transport. The influence of layering on firn gas transport is mostly untested in numerical models so far since previous firn air models were generally limited to one dimension. In particular, we will test two mechanisms by which density layering could influence
- 10 isotope ratios in firn air: (i) Layering may reduce gravitational settling of isotopes because vertical settling of isotopes is absent during horizontal transport along layers; (ii) Layering may modulate the mass-independent dispersive mixing effect of barometric pumping. Our analyses will focus on two Antarctic high-accumulation sites, WAIS Divide and Law Dome DSSW20K (Trudinger et al., 2002; Battle et al., 2011).

2 Methods

15 2.1 Governing equation and firn properties

We model 2D trace gas transport in firn by numerically solving the advection-diffusion-dispersion equation, known from hydrology (Freeze and Cherry, 1979), adapted to firn (following Schwander et al., 1993; Rommelaere et al., 1997; Trudinger et al., 1997; Severinghaus et al., 2010; Buizert et al., 2012; Kawamura et al., 2013; Buizert and Severinghaus, 2016),

$$\tilde{s} \frac{\partial q}{\partial t} = \nabla \cdot \left[\tilde{s} \mathbf{D}_m \left(\nabla q - \frac{\Delta m \mathbf{g}}{RT} q + \Omega \frac{\partial T}{\partial z} q \hat{\mathbf{k}} \right) + \tilde{s} \mathbf{D}_d \nabla q \right] - (\tilde{s} \mathbf{u}) \cdot \nabla q \quad (2)$$

- 20 with $q \equiv \delta + 1$ the ratio of any isotope to $^{28}\text{N}_2$ compared to a standard material, $\tilde{s} \equiv s_{op} \exp\left(\frac{\Delta m g}{RT} z\right)$ the pressure-corrected open porosity ($\text{m}^3 \text{m}^{-3}$), T temperature (K), Ω thermal diffusion sensitivity (K^{-1}), and \mathbf{u} the advection velocity (m s^{-1}). \mathbf{D}_m and \mathbf{D}_d are the 2D molecular diffusion and dispersion tensors ($\text{m}^2 \text{s}^{-1}$). ∇q is the concentration gradient and $\nabla \cdot$ denotes the 2D divergence operator. From left to right, the terms of Eq. (2) represent the rate of change in concentration/isotope ratio, Fickian diffusion, gravitational fractionation, thermal fractionation, dispersive mixing and advection. Since Eq. (2) is only valid for
- 25 the binary diffusion of a trace gas into a major gas, ratios of any two isotopes of masses x and y are obtained by separately simulating the transport of each isotope into the major gas $^{28}\text{N}_2$ and using the relationship

$$q_{x/y} = \frac{q_{x/28}}{q_{y/28}} \quad (3)$$

to calculate the isotope ratios of interest (Severinghaus et al., 2010).

- 30 Isotope ratios are assumed to be constant at the surface (Dirichlet boundary) and reconstructions of atmospheric CO_2 and CH_4 concentrations over the last 200 years are used to force runs of these anthropogenic tracers (see Supplementary Information

(SI)). The model time step is 3.5 days; smaller time steps make the model impractical to run due to computational costs. The bottom boundary is implemented by allowing only the advective flux to leave the domain (Neumann boundary). Diffusion and dispersive mixing cease below the COD. A periodic boundary condition is used in the horizontal direction. The horizontal extent of the model is varied between sites with differing snow accumulation rates to maintain a constant ratio of annual layer thickness to the model's spatial extent, which affects barometric pumping velocity. Firn density (Fig. 3a) is prescribed from a fit to the measured density profile at each site. Following Severinghaus et al. (2010) and Kawamura et al. (2013), empirical relationships are used to derive open and closed porosities from the density profile (Fig. 3b). The pressure-corrected open porosity \tilde{s} is assumed to be time independent.

2.2 Advection velocity and barometric pumping

The 2D velocity field \mathbf{u} is a result of a combination of (i) air migration with the firn (\mathbf{w}_{firn}), (ii) return flow of air from the firn to the atmosphere due to the gradual compression of pores (\mathbf{u}_r), and (iii) airflow resulting from barometric pumping (\mathbf{u}_b) (Figs. 3c & 4). Details on the derivation of these velocities are provided in the SI. In short, \mathbf{w}_{firn} is constrained by assuming a time-constant snow and ice mass flux at all depths. \mathbf{u}_r is calculated based on the effective export flux of air in open and closed pores at the close-off depth (COD), imposing a constant mean vertical air flux throughout the firn column (Fig. 3d) (Rommelaere et al., 1997; Severinghaus and Battle, 2006). \mathbf{u}_b is the airflow needed to re-establish hydrostatic balance in the firn in response to any surface pressure anomaly. Surface pressure variability is represented by (pseudo-) red noise, mimicking observed pressure variability at both sites. The near-coast location Law Dome is more strongly affected by storm activity than WAIS Divide with pressure variability ~ 11.2 hPa day⁻¹ compared to ~ 7 hPa day⁻¹ at WAIS Divide. \mathbf{u}_r and \mathbf{u}_b follow Darcy's law of flow through porous media (Darcy, 1856):

$$\mathbf{u} = -\frac{\kappa}{\tilde{s}\mu} \nabla P, \quad (4)$$

with ∇P the pressure gradient, κ the permeability of firn, and μ the viscosity of air (Fig. 4).

2.3 Firn layering

Idealized firn layering is implemented by forcing the vertical velocity components u_r and u_b , as well as all vertical diffusive fluxes between the grid boxes on either side of a layer to be zero. Only the advection of air with the firn (\mathbf{w}_{firn}) remains active at these grid box boundaries. Layering limits vertical gas migration and yields almost exclusively horizontal transport between layers. We assign layers an infinitesimal thickness because of the computationally limited spatial resolution of the model. Layers are repeatedly introduced at a specific depth and migrate down with the velocity of the firn. The vertical distance between layers is set to correspond to the snow accumulation of one year and the horizontal extent of layers increases linearly with depth until they cover the entire domain at the close-off depth (COD). The mean layer opening size is held proportional to the annual layer thickness to make the vertical advection velocities independent of the arbitrary horizontal extent of the model. To obtain more realistic flow fields, the permeability of layers increases gradually towards both ends of a layer.

2.4 Dispersive mixing

The dispersion tensor \mathbf{D}_d is made up of two components, (i) non-fractionating mixing of air in the SMZ and (ii) dispersive mixing caused by barometric pumping in the tortuous firn medium. First, the SMZ is commonly represented by mass-independent (“eddy”) diffusion acting in the vertical and horizontal directions. The corresponding diffusivity profile $D_{SMZ}(z)$ is prescribed as an exponential decay away from the snow-atmosphere interface (Kawamura et al., 2013). Its maximum surface value and the decay constant are chosen to match observed $\delta^{15}\text{N}$ values in the deep firn. After reaching a specified maximum depth of 8 m at WAIS Divide and 14 m at Law Dome DSSW20K, D_{SMZ} tapers linearly to zero over 2 m.

Second, airflow through any dispersive medium leads to mixing in the directions longitudinal and transverse to the flow. Because barometric pumping velocities are orders of magnitude faster than the return flow, dispersive mixing is dominated by barometric pumping. The degree of dispersive mixing in firn presumably depends on the direction of flow and differs between the longitudinal-to-flow and transverse-to-flow direction. However, the treatment of anisotropic media is complex and only one parametrization for vertical, longitudinal-to-flow dispersion in firn is currently available (Buizert and Severinghaus, 2016). Therefore, we assume that the dispersivity α of firn is isotropic and linearly dependent on the magnitude of the flow velocity vector ($v \equiv |\mathbf{u}_b + \mathbf{u}_r|$). In this case, the 2D dispersion tensor becomes

$$\mathbf{D}_d = (\alpha v + D_{SMZ}) \mathbf{I}, \quad (5)$$

with \mathbf{I} the second order identity matrix (Freeze and Cherry, 1979; Buizert and Severinghaus, 2016). The dispersion flux term in Eq. (2) simplifies to

$$\tilde{s} \mathbf{D}_d \nabla q = \tilde{s} [\alpha v + D_{SMZ}] \nabla q. \quad (6)$$

The dispersivity parametrization of Buizert and Severinghaus (2016) is based on direct measurements of cylindrical firn samples from Siple Station, Antarctica, performed by Schwander et al. (1988). The parameterization relates dispersivity to open porosity s_{op} as

$$\alpha(s_{op}) = \tilde{s} [1.26 \cdot \exp(-25.7 s_{op})]. \quad (7)$$

A factor of \tilde{s} was added to the original parameterization by Buizert and Severinghaus (2016) because α relates dispersive mixing to the velocity components u_n and w_n , that denote flow velocities per unit pore cross-section (w_{pores}). Schwander et al. (1988), however, originally measured the considerably slower bulk airflow per unit firn cross-section (i.e., $w_{bulk} = \frac{w_{pores}}{\tilde{s}}$). Since dispersivity is a scale dependent property, it is important to use parameterizations that are compatible with the resolution of the numerical model. The sample size of Schwander et al. (1988) (30 mm diameter & 50 mm length) approximately matches the resolution of our numerical model (30 × 40 mm) and thus should adequately approximate subgrid-scale (i.e., pore-scale) mixing processes that currently cannot be resolved. Spatial inhomogeneity of subgrid-scale firn dispersivity that was not captured by the sampling of Schwander et al. (1988) cannot be accounted for in the model. Dispersion on larger scales such as the interaction of flow and layers is explicitly represented in the model by the interplay of advection and diffusion. Thus, dispersive mixing is fully constrained in the model and based on empirical parameterizations that are not subject to tuning.

2.5 Molecular diffusion

The (effective) molecular diffusivity profile is established by simultaneously fitting the simulated CO₂ and CH₄ profile to real firm measurements at both sites. Effective vertical diffusivity decreases with depth to represent the subgrid-scale effect of decreasing pore connectivity and increasing firm tortuosity, which is not fully represented by the explicit macroscopic layers in our model. A spline function is used to obtain the effective vertical diffusivity profile, which decreases monotonically from the surface to zero at the COD (Fig. 5). Diffusivities for other trace gases are calculated by scaling the tuned CO₂ diffusivity by the free air diffusivity of each gas relative to CO₂ (Trudinger et al., 1997). The diffusivity tuning presents an underconstrained problem because horizontal and vertical molecular diffusivities are essentially free parameters. It is qualitatively evident from firm air sampling that horizontal connectivity/diffusivity is much higher than vertical diffusivity in deep firm, but no satisfactory quantification of this anisotropy is available. As a best guess estimate, we set horizontal molecular diffusivities equal to 10× the vertical diffusivity at the same depth. There are many degrees of freedom in tuning molecular diffusivities and our diffusivity parameterization is therefore not unique. However, sensitivity tests with equal horizontal and vertical diffusivity in the model (compensated by shorter horizontal layers) yield comparable results.

2.6 Thermal fractionation and temperature model

Finally, a 1D vertical thermal model by Alley and Koci (1990) is run separately to simulate the temperature evolution of the firm. The model is forced by a long-term surface temperature trend based on published records by Van Ommen et al. (1999); Dahl-Jensen et al. (1999); Orsi et al. (2012). A mean Antarctic seasonal cycle derived from a ~8–10-year climatology of automatic weather station observations at WAIS Divide and Law Dome (Lazzara et al., 2012) is superimposed on this trend. Alley and Koci’s temperature model is based on the heat transport equation for firm (Johnsen, 1977) with parameterizations for firm thermal properties from (Weller and Schwerdtfeger, 1977). Horizontal temperature gradients in firm are small at both sites and neglected in this study.

Considerable temperature gradients can exist in present-day firm because of recent global atmospheric warming and these gradients can lead to increased isotope thermal fractionation, in particular of $\delta^{15}\text{N}$. The sensitivity of isotopes to diffuse in response to temperature gradients is captured by the thermal diffusion sensitivity Ω . The temperature dependence of Ω is approximated as a function of the effective average temperature T in Kelvin:

$$\Omega = \frac{a}{T} - \frac{b}{T^2} \quad (8)$$

or Ω is assumed to be temperature independent if the coefficients a and b are unknown for a specific isotope ratio (Severinghaus et al., 2001). Coefficients a and b were determined experimentally for different isotope ratios by Grachev and Severinghaus (2003a, b) and Kawamura et al. (2013).

A table of all model parameters and further details of the numerical realization of 2D gas transport is provided in the SI.

3 Results

3.1 WAIS Divide

3.1.1 CO₂ and CH₄

A comparison of simulated and observed CO₂ and CH₄ profiles shows good agreement at WAIS Divide, supporting the plausi-
5 bility of our layered diffusivity parameterization (Fig. 6). In line with observations, both CO₂ and CH₄ concentrations decrease slowly with depth until ~68 m below the surface due to the gradually increasing gas age and the anthropogenic rise in atmospheric CO₂ and CH₄ concentrations. The more rapid decrease of CO₂ and CH₄ below ~68 m is explained by a much slower vertical penetration of air and a faster increase of the gas age with depth in the LIZ.

In the following discussion we will examine and compare results from four different versions of the 2D model: with or
10 without impermeable layers and with activated or deactivated barometric pumping. In versions without layering, our 2D model loses all horizontal heterogeneity and will thus be referred to as a “1D model” in what follows. Since the explicitly implemented tortuosity from layering in the 2D model affects molecular diffusion and dispersion equally it is represented by lowering the effective molecular diffusivity and dispersivity equally in the layered region of the 1D version instead. Diffusivities are tuned such that the CO₂ profiles are (nearly) identical. The small remaining deviations in CO₂ and CH₄ concentrations between
15 model versions ($< \pm 0.4$ ppm and $< \pm 9$ ppb, respectively) are illustrated in Fig. S12.

3.1.2 $\delta^{15}\text{N}$ and thermal fractionation

In all four model setups, the seasonal cycle of temperature dominates the shape of the $\delta^{15}\text{N}$ profiles in the top ~30 m (Fig. 7). Warm summer temperatures drive the migration of heavy isotopes into the colder firn below and produce a $\delta^{15}\text{N}$ summer peak just below the surface (Severinghaus et al., 2001). In contrast, a minimum of $\delta^{15}\text{N}$ occurred in this region during the previous
20 winter season when the thermal gradients were reversed. The remnants of this winter minimum are still visible in the gas record as anomalously low $\delta^{15}\text{N}$ values below the summer peak. The differences between observations and simulated $\delta^{15}\text{N}$ values in the top of the firn column are likely caused by our idealized representation of the seasonal cycle in the model.

3.1.3 Impact of reduced-permeability layers

In the layered 2D model without barometric pumping, the simulated $\delta^{15}\text{N}$ values are close to observations at the top of the
25 LIZ but continue to increase with depth (Fig. 7). This is contradicted by observational data even when the unusually low $\delta^{15}\text{N}$ values at the COD and below are not taken into consideration (near the COD, firn air sampling becomes more difficult in the field and the potential for fractionation during sampling is increased). A closer inspection of the lock-in zone in Figs. 7 and 8 reveals a zigzag pattern in the $\delta^{15}\text{N}$ profile where impermeable layers are present. Simulated isotope ratios are higher just above horizontal layers, where heavy isotopes can accumulate, and are anomalously low below layers where heavy isotopes
30 are more readily removed than supplied by gravitational settling. Gravitational settling through gaps in the layers sets up small horizontal concentration gradients that drive horizontal Fickian diffusion. Layering increases the effective travel path length

for molecules and reduces the effective vertical diffusivity by increasing the tortuosity. However, layering alone appears to be insufficient to prevent gravitational settling completely, with continued gravitational enrichment being observed in the LIZ in this model version.

Is the impact of layers on the firm trace gas profile larger for isotopes such as $\delta^{15}\text{N}$ than for anthropogenic tracers such as CO_2 , CFCs, or CH_4 ? All three gases have experienced large atmospheric variability in the industrial era. Therefore, the migration of these gases into the firm is dominated by vertical and horizontal Fickian diffusion. For $\delta^{15}\text{N}$, on the other hand, the effect of gravity is critical for transport. To answer the above question, we compare output from the layered 2D model to the 1D model without layers. We find that $\delta^{15}\text{N}$ values in the 1D and 2D model without barometric pumping are almost identical (Fig. 7). Layering in the 2D model increases the effective transport distance for CO_2 just as much as for $\delta^{15}\text{N}$ and there is no disproportional impact of layering on gravitationally fractionated isotope ratios. Differences in explicitly represented tortuosity are automatically compensated in the 1D model during tuning to the same CO_2 profile by reducing molecular diffusivities. Therefore, we conclude that layering alone cannot simultaneously explain the observed CO_2 and $\delta^{15}\text{N}$ patterns.

3.1.4 Barometric pumping and the emergence of the LIZ

$\delta^{15}\text{N}$ values simulated by the 1D and 2D model with barometric pumping are lower in the LIZ than in both model versions without barometric pumping (Fig. 7). Accounting for barometric pumping improves the agreement with observations throughout the lock-in zone. However, the reduction of gravitational fractionation is substantially stronger when layers are present. Only when both layering and barometric pumping are accounted for in the model simultaneously, does the $\delta^{15}\text{N}$ profile correctly indicate no further gravitational enrichment in the LIZ and match observations more closely. Dispersive mixing is nearly independent of molecular mass and does not lead to gravitational fractionation, but rather acts to eliminate the concentration gradients associated with gravitational settling. Although barometric pumping velocities are largest near the surface (Fig. 3c), significant dispersive mixing is generally limited to the LIZ because dispersivity of firm is inversely related to the open porosity in the parameterization of Buizert and Severinghaus (2016) and dispersion is overwhelmed by molecular diffusion in the DZ. Furthermore, molecular diffusivities drop rapidly in the LIZ in the model (Fig. 5). Because dispersion provides an additional transport mechanism for trace species, even less molecular diffusion is needed to match observed CO_2 and CH_4 concentrations in the LIZ when barometric pumping is active. Layering amplifies the importance of barometric pumping because gravitational fractionation between annual layers is restricted into the small gaps in the LIZ (Fig. 8). Narrow pathways amplify barometric pumping flow velocities and thus dispersive mixing in these regions (Fig. 4), thus overwhelming the influence of gravitational fractionation more readily than in the 1D model. This effect is responsible for the larger differences between the $\delta^{15}\text{N}$ profiles obtained from the two model versions with barometric pumping in Fig. 7. The strength of dispersive mixing in our layered 2D model is physically motivated; thus, barometric pumping and layering together lead to a more natural emergence of the $\delta^{15}\text{N}$ -defined lock-in zone in the 2D model.

3.1.5 The surface mixed zone depth

We estimate the depth of the SMZ at WAIS Divide to be ~ 2.8 m. Multiple different procedures have been used to estimate SMZ thickness in the past, many of which rely on $\delta^{15}\text{N}$ data in the deep firn near the LIZ (Battle et al., 2011). However, if the deep firn is affected by dispersive mixing due to barometric pumping, these estimates may be falsely attributing some fraction of the dispersive mixing in the deep firn to the SMZ. To address this problem, we follow the method of Severinghaus et al. (2001) in calculating SMZ thickness. This approach compares the depth where $\delta^{15}\text{N}$ reaches a certain value in two different model configurations with zero and non-zero values of D_{SMZ} . Thermal effects are neglected. The first setup is the 2D model with barometric pumping as presented above but the dispersivity is set to zero everywhere without retuning the model. The SMZ thickness is calculated from the depth difference between this model run and a second model run where barometric pumping is deactivated, $D_{SMZ} = 0$, and thus only advection and gravitational fractionation shape the profile of $\delta^{15}\text{N}$. Our depth estimate of 2.8 m is within the range of values from 1.4 to 5.2 m published previously (Battle et al., 2011).

3.2 Law Dome DSSW20K

At Law Dome DSSW20K, the firn thickness is ~ 20 m less than at WAIS Divide. Accumulation rates are comparable, but annual-mean temperatures are ~ 10 K warmer. The SMZ is slightly deeper and barometric pumping is stronger at Law Dome, yielding more near-surface and dispersive mixing. Constraining the SMZ depth at DSSW20K is more difficult because fewer $\delta^{15}\text{N}$ measurements are available for this site, and their associated uncertainty is, at ± 15 per meg, much larger than at the more recently sampled WAIS Divide site (Trudinger et al., 2002). Molecular diffusion generally takes a less important role at DSSW20K and molecular diffusivities obtained by tuning are about half or less than those at WAIS Divide for most of the firn column. Thermal fractionation has a weaker impact on the isotope record near the surface at Law Dome due to the smaller amplitude of the seasonal cycle and stronger near-surface mixing compared to WAIS Divide. Figures of molecular diffusivity, advection velocities and other firn properties at site DSSW20K are provided in the SI.

Simultaneously matching the $\delta^{15}\text{N}$, CO_2 and CH_4 profile at Law Dome DSSW20K has proven difficult in the past (Trudinger et al., 2002; Buizert and Severinghaus, 2016). Simulated $\delta^{15}\text{N}$ in the LIZ is typically substantially higher than in observations. Buizert and Severinghaus (2016) suggested that barometric pumping in the deep firn may be able to reconcile this contradiction. However, the mixing obtained from theoretical predictions was insufficient to achieve a satisfactory fit. Buizert and Severinghaus (2016) hypothesized that firn layering may play a critical role in amplifying the impact of barometric pumping. The authors used an idealized eddy and molecular diffusivity profile in the deep firn to simulate the effect of layers on firn air transport. Using these diffusivity profiles, they were able to obtain good agreement with observed $\delta^{15}\text{N}$, CH_4 and $^{14}\text{CO}_2$. Our 2D model includes an explicit representation of layering and places similar physical constraints on barometric pumping as the 1D model of Buizert and Severinghaus (2016). The model is tuned to optimize agreement with CO_2 and CH_4 and the patterns of both profiles are reproduced correctly (Fig. 9). But the disagreement between modeled and observed $\delta^{15}\text{N}$ in the deep firn remains despite barometric pumping producing substantial non-fractionating dispersive mixing in the region (Fig. 10). Simulated $\delta^{15}\text{N}$ values diverge from observations at ~ 38 m, where gravitational enrichment seems to stop in observations but continues

in the model. In contrast, the LIZ, as defined by CO₂ and CH₄, only starts at roughly 43 m depth. Such an early onset of dispersive mixing is not supported by the dispersivity parameterization. However, only the longitudinal-to-flow mixing in the vertical direction at Siple Station was used to develop the firm dispersivity parameterization, and the use of this parameterization may be inappropriate at Law Dome DSSW20K (Buizert and Severinghaus, 2016). Moreover, dispersivity typically differs in the horizontal and vertical as well as the longitudinal- and the traverse-to-flow directions, an effect that is not accounted for in this study because of a lack of observational evidence to constrain anisotropic dispersivity.

4 Discussion

4.1 Differential kinetic isotope fractionation

Isotope ratios in firm typically do not reach values as high as predicted from gravitational equilibrium due to the influence of advection and non-fractionating dispersive mixing (Trudinger et al., 1997; Kawamura et al., 2013; Buizert and Severinghaus, 2016). Advection and mass-independent mixing transport less-fractionated air down in the firm column and act to counterbalance the enrichment of heavy isotopes by gravitational fractionation. As a result, all isotope ratios fall below the gravitational settling line δ_{grav} (Fig. 11) but the magnitude of the deviation depends on the specific isotope pair.

The magnitude of disequilibrium of different isotope and elemental ratios is quantified here by defining the (mass-normalized) kinetic fractionation ϵ' relative to $\delta^{15}\text{N}$ (Kawamura et al., 2013) as

$$\epsilon'_{x/y} \equiv \frac{1}{1000 \times \Delta m_{x/y}} \ln \left(\frac{q_{x/28}}{q_{y/28}} \right) - \ln(q_{15\text{N}}), \quad (9)$$

where $\Delta m_{x/y}$ is the mass difference of isotopes x and y . This definition is similar to the ⁸⁶Kr excess terminology introduced by Buizert and Severinghaus (2016) but ϵ' is given in the more precise $\ln(q)$ -notation and uses $\delta^{15}\text{N}$ as reference instead of $\delta^{40}\text{Ar}/^{36}\text{Ar}$. To calculate $\epsilon'_{x/y}$, isotope ratios must have been previously corrected for the influence of thermal fractionation either through combined Ar and N₂ isotope measurements on firm air (Grachev and Severinghaus, 2003a, b) or, as done here, by removing temperature effects with a suitable firm air transport model (Fig. 12).

The degree of disequilibrium, represented by ϵ' , is caused by differential kinetic isotope fractionation. Heavy, slow-diffusing isotopes approach gravitational equilibrium more slowly than lighter, faster-diffusing isotopes. Therefore, slow-diffusing isotopes experience larger kinetic fractionation (i.e., deviations from gravitational equilibrium) in regimes with non-zero advection or dispersion. Consequently, ϵ' is more negative for heavier, slower diffusing isotopes. On its own, this rule of thumb cannot fully explain the pattern of ratios containing two different elements, such as ¹³²Xe/²⁸N₂. The magnitude of disequilibrium in such mixed-element ratios is further discussed in Appendix B.

In the DZ, ϵ' decreases almost linearly with depth, while within the SMZ and LIZ ϵ' changes much more rapidly. Where molecular diffusivity is zero, ϵ' remains constant. This pattern is explained by the relative importance of advection and dispersive mixing compared to molecular diffusion in different regions of the firm column. The Péclet number (Pe) traditionally quantifies the ratio of the advective to the diffusive transport and is here defined as the ratio of the diffusive to the advective time scale (τ_{D_m} and τ_{adv}). We add the time scale of dispersive mixing (τ_{D_e}) to the numerator because the effect of advection

and dispersive mixing on the isotope profiles is very similar although the physics differ (Kawamura et al., 2013).

$$Pe \equiv \frac{\tau_{adv} + \tau_{D_e}}{\tau_{D_m}} \sim \frac{\frac{W}{L} + \frac{D_e}{L^2}}{\frac{D_m}{L^2}} \sim \frac{WL + D_e}{D_m}, \quad (10)$$

where $L = 1$ m is the characteristic length scale of firn air transport, and D_m , W and D_e are characteristic values of the molecular diffusivity, the time mean vertical advection velocity, and the vertical dispersive or convective mixing at that depth, respectively.

This modified Péclet number varies in the model by many orders of magnitude through the firn column at WAIS Divide with peak values in the SMZ and the deep firn (Fig. 13). High modified Péclet numbers in the SMZ are caused primarily by large D_e values, and high modified Péclet numbers in the LIZ are mostly the result of low molecular diffusivities. Kawamura et al. (2013) showed analytically that relative kinetic isotope fractionation depends on the ratio of eddy diffusivity to molecular diffusivity, but the role of advection was neglected due to near-zero accumulation rates at the Megadunes site. The absolute difference in kinetic isotope fractionation (i.e., ϵ') should be greatest when the product of the modified Péclet numbers of both isotopes is near one. In line with these theoretical predictions, we observe almost no further isotopic enrichment of $\delta^{15}\text{N}$ in the lock-in zone when barometric pumping is included in the model and $Pe \gg 1$ (Figs. 7 & 13). The largest changes of ϵ' occur in the 2D model when the product of the modified Péclet numbers is within approximately 1–2 orders of magnitude of unity. This region is illustrated by the vertical gray bar in Fig. 13, which contains the SMZ as well as the beginning of the LIZ where non-fractionating mixing is of similar magnitude as molecular diffusion.

With active barometric pumping and centimeter-scale layering, the product of the modified Péclet numbers at the bottom of the LIZ becomes so large that ϵ' stops to decrease entirely in our model. If barometric pumping is neglected instead, the modified Péclet numbers in the layered 2D model are considerably lower in the LIZ and some gravitational and kinetic fractionation persists (i.e., $\delta^{15}\text{N}$ and ϵ' continue to change gradually). Therefore, barometric pumping leads to slightly weaker rather than stronger differential kinetic fractionation at the COD of WAIS Divide in contrast to expectations (Buizert and Severinghaus, 2016). Furthermore, layering and barometric pumping in the model seem to be insufficient to obtain the full ~ 5 – 23 per meg per amu range of ϵ'_{Kr} values measured in the WAIS Divide ice core record (WAIS Divide Project Members, 2015; Bereiter et al., 2018). Instead, other, unresolved (i.e., subgrid-scale) processes may be the reason for the large observed disequilibrium. Establishing a straightforward relationship between disequilibrium and surface pressure variability using firn air models alone may not be possible without more observational data.

4.2 Diffusive fractionation

Strong kinetic isotope fractionation can also be observed for trace gases that experience large changes in the atmospheric mixing ratio while the atmospheric isotope ratios remain constant (Trudinger et al., 1997; Buizert et al., 2013). As the concentration of a trace gas increases, isotopologues of the gas migrate into the firn column at different speeds because of small differences in their masses and diffusivities. This results in a relative depletion of the slower diffusing isotopologue with depth called diffusive fractionation (Trudinger et al., 1997). During periods of abrupt CH_4 change, diffusive fractionation commonly amounts to a relevant correction in ice core studies (Trudinger et al., 1997; Buizert et al., 2013). Diffusive fractionation of $\delta^{13}\text{C}-\text{CH}_4$ is strong,

and poorly constrained by models, to the degree that it prohibits the reliable atmospheric reconstruction of this parameter from firn air measurements (Sapart et al., 2013). Since diffusive fractionation is a type of kinetic fractionation, it can be tested in our model. We assume a constant atmospheric $^{13}\text{C}/^{12}\text{C}$ isotope ratio of 1.1147302 ‰ for CO_2 (i.e., $\delta^{13}\text{C}\text{-CO}_2 = -8$ ‰) and 1.0709052 ‰ for CH_4 (i.e., $\delta^{13}\text{C}\text{-CH}_4 = -47$ ‰), respectively. Thermal fractionation and gravitational settling are neglected to isolate the impact of the atmospheric mixing ratio change. The model including barometric pumping calculates $\delta^{13}\text{C}\text{-CO}_2$ and $\delta^{13}\text{C}\text{-CH}_4$ values depleted by up to ~ 0.2 ‰ and ~ 2 ‰ relative to the atmosphere in the WAIS Divide LIZ at the time of firn air sampling (Fig. 14). Without barometric pumping, delta values are notably higher because molecular diffusion is stronger, and the dispersive mixing no longer smooths out the profile in the deep firn.

4.3 Predicting disequilibrium

Past mean ocean temperature can be estimated from the noble gas concentrations in ice core bubbles (Headly and Severinghaus, 2007; Ritz et al., 2011; Bereiter et al., 2018). On glacial-interglacial timescales, atmospheric concentrations of noble gases are primarily controlled by gas dissolution in the ocean. Because the temperature sensitivity of solubility is different for each gas, measurements of noble gas ratios in ice cores can be used to obtain a signal of integrated ocean temperature. However, as for any gas, the trace gas concentrations in bubbles must first be corrected for alterations of the atmospheric signal in the firn. In a recently published deglacial mean ocean temperature reconstruction, the WAIS Divide noble gas ice core record was corrected for gravitational fractionation and thermal fractionation using $\delta^{40}\text{Ar}/^{36}\text{Ar}$ measurements and a firn temperature gradient estimate (Bereiter et al., 2018). The authors further noted that different degrees of deviation from gravitational equilibrium (i.e., disequilibrium) can bias the gravitational fractionation correction applied to the raw noble gas record, which may lead to a cold bias of $\sim 0.3^\circ\text{C}$ in Holocene and LGM temperatures. Disequilibrium effects of -287.5 per meg for Kr/N_2 , -833.3 per meg for Xe/N_2 and -545.7 per meg for Xe/Kr simulated by our model correspond to absolute temperature biases of 0.33°C , 0.41°C , and 0.45°C , respectively, following the method of Bereiter et al. (2018). Because the magnitude of disequilibrium depends on firn properties and accumulation rate, glacial-interglacial changes in environmental boundary conditions may also affect the magnitude of disequilibrium in firn and thus the size of the relative deglacial temperature change estimated from noble gases.

In an attempt to compensate implicitly for disequilibrium effects and gravitational settling at the same time, it has been suggested that the elemental ratios Kr/N_2 and Xe/N_2 in bubbles should be corrected by subtracting krypton or xenon isotope ratios, respectively (Headly, 2008). This would assume that krypton and xenon isotopes may be influenced similarly by the processes responsible for creating disequilibrium in Kr/N_2 and Xe/N_2 . Therefore, this approach may compensate for disequilibrium effects and gravitational settling simultaneously, but it has been untested in models so far. The ϵ' values simulated here allow us to evaluate this method quantitatively. We use a linear fit to predict $\epsilon'_{\text{Kr}/\text{N}_2}$ from ϵ'_{Kr} . The linear fit yields good agreement with the modeled ϵ'_{Kr} over the whole firn column ($R^2 > 0.998$), indicating that the scaling between ϵ' values is nearly independent of depth. We find that (mass-normalized) $\epsilon'_{\text{Kr}/\text{N}_2}$ should be approximately 75 ‰ of (mass-normalized) ϵ'_{Kr} at the WAIS Divide site. Scaling relationships for other isotope and element pairs are shown in Table 1 and are equally robust. Moreover, our results show that the source of disequilibrium is irrelevant for the correction for the macroscopic processes represented in our model. Advection and convective or dispersive mixing show the same scaling relationships for ϵ' . At Law Dome DSSW20K,

the calculated ratio of ϵ'_{Kr/N_2} and ϵ'_{Kr} is at 75.9 % almost identical to the result at WAIS Divide. Sensitivity tests with the 1D analytical model presented in Appendix A demonstrate that the disequilibrium scaling relationship between Kr isotopes and Kr/N₂ is robust to within ± 5 % over a wide parameter range of molecular diffusivity, eddy diffusivity and advection velocity. Uncertainties become largest in the extreme case when ϵ'_{Ar} , the lowest simulated ϵ' value, is used to predict $\epsilon'_{Xe/Kr}$, the highest simulated ϵ' value, but they never exceed ± 25 %.

This suggests that the same scaling relationship between ϵ'_{Kr/N_2} and ϵ'_{Kr} may be assumed to hold for any ice core site without introducing large biases. ϵ'_{Kr} and ϵ'_{Xe} from combined measurements of $\delta^{15}N$, $\delta^{86}Kr/^{82}Kr$ and $\delta^{136}Xe/^{129}Xe$ in ice cores could be used to predict the disequilibrium effects on noble elemental ratios (i.e., ϵ'_{Kr/N_2} , ϵ'_{Xe/N_2} and $\epsilon'_{Xe/Kr}$) and allows us to make a gas-specific gravitational correction. Although predicted ϵ'_{Kr} values at WAIS Divide are close to the current analytical uncertainty of the $^{86}Kr/^{82}Kr$ measurement, correcting for kinetic fractionation and disequilibrium will become advisable with future improvements in precision and may improve mean ocean temperature reconstructions.

5 Conclusions

We developed a two-dimensional firn air transport model that explicitly represents tortuosity in the firn column through migrating layers of reduced permeability. The idealized representation of firn layering is physically motivated and may illustrate the impact of firn density anomalies (i.e., summer vs winter firn or wind crusts) on gas transport. The model also accounts for thermal fractionation, a surface mixed zone, and surface pressure-forced barometric pumping. Dispersive mixing as a result of barometric pumping is constrained in the model by previously published parameterizations and not subject to tuning. Simulations of the $\delta^{15}N$ profile at WAIS Divide show that extensive horizontal diffusion through the tortuous firn structure is required by the discontinuous layers. This limits the effective vertical diffusion of gases at depth. However, layering alone does not fully prevent gravitational enrichment of isotopes in the deep firn. Similarly, the effect of barometric pumping alone is insufficient to obtain agreement with observations. The combination of barometric pumping with layering, in contrast, leads to amplified dispersive mixing. This is due to high velocity focusing in layer openings and leads to a more natural emergence of a lock-in zone in the model.

Previous studies have shown that downward advection, convective mixing and dispersive mixing all hinder trace gases in reaching the isotope ratios expected from gravitational settling (e.g., Severinghaus et al., 2010; Kawamura et al., 2013; Buizert and Severinghaus, 2016). Kinetic fractionation is strongest for slow-diffusing gases and increases with firn column depth. Our numerical experiments show that barometric pumping leads to increased isotopic disequilibrium in the firn column. However, our simulations fail to account for the full range of ^{86}Kr excess observed in the WAIS Divide core, as well as for the relatively weak $\delta^{15}N$ enrichment seen at DSSW20K, suggesting that these effects are not caused by the presence of layering (as previously suggested) and that their origin must be sought elsewhere. We further find robust scaling relationships between the magnitude of disequilibrium in different noble gas isotope and elemental ratios. Our results suggest that, to first order, these scaling relationships are independent of depth in the firn column and independent of the reason for disequilibrium for the

process represented in the model (i.e., dispersive mixing, advection or convective mixing). Thus, a correction that accounts for differential kinetic fractionation may be applied to observed noble gas ratios in the reconstruction of mean ocean temperature.

Code availability. Matlab code for the 2D firn air transport model is available from the corresponding author upon reasonable request.

Appendix A: Appendix A: An analytical solution for simplified firn air transport

- 5 Here, we seek an analytical solution to the following idealized scenario of firn air transport: firn air advection, diffusion, and dispersion in one dimension. In this case, vertical trace gas migration relative to the major gas nitrogen is governed by

$$\tilde{s} \frac{\partial q}{\partial t} = \frac{\partial}{\partial z} \left[\tilde{s} D_m \left(\frac{\partial q}{\partial z} - \frac{\Delta m g}{RT} q + \Omega \frac{\partial T}{\partial z} q \right) + \tilde{s} D_e \frac{\partial q}{\partial z} \right] - \tilde{s} w \frac{\partial q}{\partial z}, \quad (\text{A1})$$

- with D_m and D_e the molecular and eddy diffusivity ($\text{m}^2 \text{s}^{-1}$) and w the effective vertical air advection velocity due to snow accumulation and pore compression (m s^{-1}) (e.g., Schwander et al., 1993; Rommelaere et al., 1997; Trudinger et al., 1997; Severinghaus et al., 2010; Buizert et al., 2012; Kawamura et al., 2013). The five terms on the right-hand side of Eq. (A1) represent Fickian diffusion, gravitational settling, thermal fractionation, mass-independent dispersion and gas advection (from left to right). A Dirichlet boundary condition is chosen at the top of the firn column and represents the well-mixed atmosphere (i.e., $q(0) \equiv 0$). The bottom boundary condition is given by a Neumann boundary condition allowing only an advective flux to leave the domain ($\tilde{s} (D_m + D_e) \frac{\partial q}{\partial z} - s D_m \left(\frac{\Delta m g}{RT} - \Omega \frac{\partial T}{\partial z} \right) q \equiv 0$ @ $z = z(\text{COD})$).
- 15 Assuming steady-state and neglecting changes of \tilde{s} , D_m , D_e and w with depth, Eq. (A1) reduces to (Severinghaus et al., 2010)

$$\frac{\partial q}{\partial t} \equiv 0 = (D_m + D_e) \frac{\partial^2 q}{\partial z^2} - D_m (G - \mathcal{T}) \frac{\partial q}{\partial z} - w \frac{\partial q}{\partial z}, \quad (\text{A2})$$

where $G \equiv \frac{\Delta m g}{RT}$ and $\mathcal{T} \equiv \Omega \frac{\partial T}{\partial z}$ represent the constants in the gravitational and thermal fractionation term.

The solution to Eq. (A2) yields trace gas profiles above the COD in delta notation

$$20 \quad \delta = \frac{\exp\left(\frac{D_m(G-\mathcal{T})+w}{D_m+D_e} z\right) - 1}{\frac{w}{D_m(G-\mathcal{T})} \exp\left(\frac{D_m(G-\mathcal{T})+w}{D_m+D_e} z_{\text{COD}}\right) + 1}, \quad (\text{A3})$$

where $z_{\text{COD}} \equiv z(\text{COD})$ (Fig. S2). δ values below the COD are constant. Note that Eq. (A2) only applies to trace gas transport into N_2 , not to transport of one trace gas into another trace gas, as discussed in the text. Because $\delta^{15}\text{N}$ only requires calculating the transport of the trace gas $^{15}\text{N}^{14}\text{N}$ into the major gas $^{28}\text{N}_2$, the equation can be used as is to calculate $\delta^{15}\text{N}$.

- By evaluating some extreme cases, Eq. (A3) illustrates a few key points about trace gas transport of $\delta^{15}\text{N}$ in firn. Under a large negative temperature gradient (i.e., atmospheric warming, $\mathcal{T} \rightarrow -\infty$), $\delta \rightarrow \infty$ and thermally sensitive gases are enriched in the firn because the numerator grows faster than the denominator. Similarly, heavier gases ($G \rightarrow \infty$) are more strongly fractionated ($\delta \rightarrow \infty$) than lighter gases assuming they have the same molecular diffusivity. Advection ($w \rightarrow \infty$) and eddy

mixing ($D_e \rightarrow \infty$) prevent the system from reaching the trace gas concentrations expected from gravitational settling and ultimately force concentrations to be constant ($\delta \rightarrow 0$). A lack of molecular diffusion ($D_m \rightarrow 0$) leads to the same result ($\delta \rightarrow 0$). Naturally, Eq. (A3) reduces to the profile of a gravitationally settled gas (i.e., Eq. (1)) when $w \rightarrow 0$ and $D_e \rightarrow 0$.

Appendix B: Appendix B: Differential kinetic isotope fractionation in ratios of two different elements

- 5 Here we revisit the relative disequilibrium for ratios of two elements as seen in Figs. 11 and 12. First, recall the definition of ϵ' for a ratio of isotopes x and y (indicated by their nominal atomic masses)

$$\epsilon'_{x/y} \equiv \frac{10^{-3}}{m_x - m_y} \ln(q_{x/y}) - \ln(q_{29/28}) = \ln\left(\frac{q_{x/y}^{\frac{10^{-3}}{m_x - m_y}}}{q_{29/28}}\right). \quad (\text{B1})$$

Equation (3) shows that $q_{x/y}$ is the ratio of q values calculated for the transport of each isotope into $^{28}\text{N}_2$ ($q_{x/28}$ and $q_{y/28}$). $q_{x/28}$ (or $q_{y/28}$) may also be expressed in reference to nitrogen using the ϵ' value for the isotope

$$10 \frac{10^{-3}}{m_x - m_{28}} \ln(q_{x/28}) = \ln(q_{29/28}) + \epsilon'_{x/28} \rightarrow q_{x/28} = \left(q_{29/28} \cdot \exp(\epsilon'_{x/28})\right)^{10^3 \times (m_x - m_{28})} \quad (\text{B2})$$

Note that ϵ' by definition is already mass-normalized. It follows from Eqs. (3), (B1) and (B2) that

$$\epsilon'_{x/y} = \ln\left(\frac{\left(\frac{q_{x/28}}{q_{y/28}}\right)^{\frac{10^{-3}}{m_x - m_y}}}{q_{29/28}}\right) = \ln\left(\frac{\left(\frac{\left(q_{29/28} \cdot \exp(\epsilon'_{x/28})\right)^{m_x - m_{28}}}{\left(q_{29/28} \cdot \exp(\epsilon'_{y/28})\right)^{m_y - m_{28}}}\right)^{\frac{1}{m_x - m_y}}}{q_{29/28}}\right). \quad (\text{B3})$$

Equation (B3) may be rewritten to yield

$$\epsilon'_{x/y} = \frac{m_x - m_{28}}{m_x - m_y} \left[\ln(q_{29/28}) + \epsilon'_{x/28} \right] - \frac{m_y - m_{28}}{m_x - m_y} \left[\ln(q_{29/28}) + \epsilon'_{y/28} \right] - \ln(q_{29/28}). \quad (\text{B4})$$

- 15 Because the terms containing $q_{29/28}$ cancel, we obtain a straightforward expression to find ϵ' for any isotope ratio from the ϵ' of two nuclides relative to $^{28}\text{N}_2$

$$\epsilon'_{x/y} = \frac{m_x - m_{28}}{m_x - m_y} \epsilon'_{x/28} - \frac{m_y - m_{28}}{m_x - m_y} \epsilon'_{y/28}. \quad (\text{B5})$$

- Analysis of this relationship reveals that disequilibrium should most strongly affect ratios of two heavy isotopes, such as $^{132}\text{Xe}/^{84}\text{Kr}$, because heavy elements diffuse slower than N_2 (i.e., $\epsilon'_{x/28} \ll 0$) and the mass weighting factor is larger in the first than in the second term (i.e., $\frac{m_x - m_{28}}{m_x - m_y} \gg \frac{m_y - m_{28}}{m_x - m_y}$). Although this equation can theoretically predict ϵ' of any isotope ratio from ϵ' of the two isotopes x and y relative to $^{28}\text{N}_2$ (i.e., $\epsilon'_{x/28}$ and $\epsilon'_{y/28}$), in practice, this approach will not allow correcting for differential kinetic isotope fractionation. $\epsilon'_{x/28}$ cannot be measured directly and the atmospheric ratio of the noble gas x to nitrogen is not constant over long timescales. Thus, $\epsilon'_{x/28}$ will not only be affected by disequilibrium but will also be influenced

by atmospheric variability resulting from gas specific solubility differences (i.e., precisely the mean ocean temperature signals we attempt to reconstruct). Instead we suggest that the scaling relationships provided in Sect. 4.3 can be used to predict the ϵ' of noble gas elemental ratios.

Competing interests. The authors declare that they have no conflict of interest.

- 5 *Acknowledgements.* We would like to thank Jakob Keck, Alan Seltzer and Ian Eisenman for providing computational resources and insightful discussions on the numerical implementation of firn air transport. Sarah Shackleton has provided helpful comments on the importance of disequilibrium in mean ocean temperature reconstruction. This work was supported by NSF grants PLR-1543229 and PLR-1543267.

References

- Alley, R. B. and Koci, B. R.: Recent warming in central Greenland?, *Annals of Glaciology*, 14, 6–8, 1990.
- Battle, M. O., Severinghaus, J. P., Sofen, E. D., Plotkin, D., Orsi, A. J., Aydin, M., Montzka, S. A., Sowers, T., and Tans, P. P.: Controls on the movement and composition of firn air at the West Antarctic Ice Sheet Divide, *Atmospheric Chemistry and Physics*, 11, 11 007–11 021, <https://doi.org/10.5194/acp-11-11007-2011>, 2011.
- Bereiter, B., Shackleton, S., Baggenstos, D., Kawamura, K., and Severinghaus, J.: Mean global ocean temperatures during the last glacial transition, *Nature Publishing Group*, 553, 39–44, <https://doi.org/10.1038/nature25152>, <http://dx.doi.org/10.1038/nature25152>, 2018.
- Buizert, C. and Severinghaus, J. P.: Dispersion in deep polar firn driven by synoptic-scale surface pressure variability, *The Cryosphere*, 10, 2099–2111, <https://doi.org/10.5194/tc-2016-148>, 2016.
- 10 Buizert, C., Martinerie, P., Petrenko, V. V., Severinghaus, J. P., Trudinger, C. M., Witrant, E., Rosen, J. L., Orsi, A. J., Rubino, M., Etheridge, D. M., Steele, L. P., Hogan, C., Laube, J. C., Sturges, W. T., Levchenko, V. A., Smith, A. M., Levin, I., Conway, T. J., Dlugokencky, E. J., Lang, P. M., Kawamura, K., Jenk, T. M., White, J. W. C., Sowers, T., Schwander, J., and Blunier, T.: Gas transport in firn: Multiple-tracer characterisation and model intercomparison for NEEM, Northern Greenland, *Atmospheric Chemistry and Physics*, 12, 4259–4277, <https://doi.org/10.5194/acp-12-4259-2012>, 2012.
- 15 Buizert, C., Sowers, T., and Blunier, T.: Assessment of diffusive isotopic fractionation in polar firn, and application to ice core trace gas records, *Earth and Planetary Science Letters*, 361, 110–119, <https://doi.org/10.1016/j.epsl.2012.11.039>, 2013.
- Colbeck, S.: Air Movement in Snow due to Windpumping, *Journal of Glaciology*, 35, 209–213, 1989.
- Craig, H., Horibe, Y., and T., S.: Gravitational separation of gases and isotopes in polar ice caps, *Science*, 242, 1675–1678, 1988.
- Dahl-Jensen, D., Morgan, V. I., and Elcheikh, A.: Monte Carlo inverse modelling of the Law Dome (Antarctica) temperature profile, *Annals of Glaciology*, 29, 145–150, <https://doi.org/10.3189/172756499781821102>, 1999.
- 20 Darcy, H.: *Les Fontaines Publiques de la Ville de Dijon*, Victor Dalmont, Paris, 1856.
- Dlugokencky, E. J., Lang, P. M., Crotwell, A. M., Mund, J. W., Crotwell, M. J., and Thoning, K. W.: Atmospheric Methane Dry Air Mole Fractions from the NOAA ESRL Carbon Cycle Cooperative Global Air Sampling Network, 1983-2015, Version: 2016-07-07, 2016a.
- Dlugokencky, E. J., Lang, P. M., Mund, J. W., Crotwell, A. M., Crotwell, M. J., and Thoning, K. W.: Atmospheric Carbon Dioxide Dry Air Mole Fractions from the NOAA ESRL Carbon Cycle Cooperative Global Air Sampling Network, 1968-2015, Version: 2016-08-30, 2016b.
- 25 Etheridge, D. M., Steele, L. P., Langenfelds, R. L., Francey, R. J., Barnola, J. M., and Morgan, V. I.: Natural and anthropogenic changes in atmospheric CO₂ over the last 1000 years from air in Antarctic ice and firn, *Journal of Geophysical Research-Atmospheres*, 101, 4115–4128, <https://doi.org/10.1029/95JD03410>, 1996.
- 30 Etheridge, D. M., Steele, L. P., Francey, R. J., and Langenfelds, R. L.: Atmospheric methane between 1000 A.D. and present: Evidence of anthropogenic emissions and climatic variability, *Journal of Geophysical Research*, 103, 15 979, <https://doi.org/10.1029/98JD00923>, 1998.
- Freeze, R. and Cherry, J.: *Groundwater*, Prentice-Hall, Inc., Englewood Cliffs, New Jersey, 1979.
- Grachev, A. and Severinghaus, J. P.: Laboratory determination of thermal diffusion constants for ²⁹N₂ /²⁸N₂ in air at temperatures from -60 to 0° C for reconstruction of magnitudes of abrupt climate changes using the ice core fossil – air paleothermometer, *Geochimica et cosmochimica Acta*, 67, 345–360, 2003a.
- 35

- Grachev, A. M. and Severinghaus, J. P.: Determining the Thermal Diffusion Factor for $^{40}\text{Ar}/^{36}\text{Ar}$ in Air To Aid Paleoreconstruction of Abrupt Climate Change, *The Journal of Physical Chemistry A*, 107, 4636–4642, <https://doi.org/10.1021/jp027817u>, 2003b.
- Headly, M.: Krypton and xenon in air trapped in polar ice cores: paleo-atmospheric measurements for estimating past mean ocean temperature and summer snowmelt frequency, Phd dissertation, University of California, San Diego, 2008.
- 5 Headly, M. A. and Severinghaus, J. P.: A method to measure Kr/N_2 ratios in air bubbles trapped in ice cores and its application in reconstructing past mean ocean temperature, *Journal of Geophysical Research*, 112, 1–12, <https://doi.org/10.1029/2006JD008317>, 2007.
- Hörhold, M. W., Laepple, T., Freitag, J., Bigler, M., Fischer, H., and Kipfstuhl, S.: On the impact of impurities on the densification of polar firn, *Earth and Planetary Science Letters*, 325–326, 93–99, <https://doi.org/10.1016/j.epsl.2011.12.022>, 2012.
- Johnsen, S. J.: Stable isotope profiles compared with temperature profiles in firn with historical temperature records, *Isotopes and Impurities in Snow and Ice*, pp. 388–392, 1977.
- 10 Kawamura, K., Severinghaus, J. P., Albert, M. R., Courville, Z. R., Fahnestock, M. A., Scambos, T. A., Shields, E., and Shuman, C. A.: Kinetic fractionation of gases by deep air convection in polar firn, *Atmospheric Chemistry and Physics*, 13, 11 141–11 155, <https://doi.org/10.5194/acp-13-11141-2013>, 2013.
- Keeling, C. D., Stephen, C., Piper, S. C., Bacastow, R. B., Wahlen, M., Whorf, T. P., Heimann, M., and Meijer, H. A.: Exchanges of atmospheric CO_2 and $^{13}\text{CO}_2$ with the terrestrial biosphere and oceans from 1978 to 2000., *Global Aspects*, SIO Reference Series. Scripps Institution of Oceanography, San Diego, 01-06, 83–113, <https://doi.org/10.1007/b138533>, 2001.
- 15 Lazzara, M. A., Weidner, G. A., Keller, L. M., Thom, J. E., and Cassano, J. J.: Antarctic Automatic Weather Station Program: 30 Years of Polar Observation, *Bulletin of the American Meteorological Society*, 93, 1519–1537, <https://doi.org/10.1175/BAMS-D-11-00015.1>, 2012.
- Lüthi, D., Le Floch, M., Bereiter, B., Blunier, T., Barnola, J.-M., Siegenthaler, U., Raynaud, D., Jouzel, J., Fischer, H., Kawamura, K., and Stocker, T. F.: High-resolution carbon dioxide concentration record 650,000–800,000 years before present., *Nature*, 453, 379–382, <https://doi.org/10.1038/nature06949>, 2008.
- 20 Mitchell, L. E., Buizert, C., Brook, E. J., Breton, D. J., Fegyveresi, J., Baggenstos, D., Orsi, A., Severinghaus, J., Alley, R. B., Albert, M., Rhodes, R. H., McConnell, J. R., Sigl, M., Maselli, O., Gregory, S., and Ahn, J.: Observing and modeling the influence of layering on bubble trapping in polar firn, *Journal of Geophysical Research Atmospheres*, 120, 2558–2574, <https://doi.org/10.1002/2014JD022766>, 2015.
- 25 Orsi, A. J., Cornuelle, B. D., and Severinghaus, J. P.: Little Ice Age cold interval in West Antarctica: Evidence from borehole temperature at the West Antarctic Ice Sheet (WAIS) Divide, *Geophysical Research Letters*, 39, 1–7, <https://doi.org/10.1029/2012GL051260>, 2012.
- Orsi, A. J., Kawamura, K., Fegyveresi, J. M., Headly, M. A., Alley, R. B., and Severinghaus, J. P.: Differentiating bubble-free layers from Melt layers in ice cores using noble gases, *Journal of Glaciology*, 61, 585–594, <https://doi.org/10.3189/2015JoG14J237>, 2015.
- 30 Petit, R. J., Jouzel, J., Raynaud, D., Barkov, N. I., Barnola, J.-M., Basile, I., Bender, M., Chappellaz, J., Davis, M., Delaygue, G., Delmotte, M., Kotlyakov, V. M., Legrand, M., Livinkov, V. Y., Lorius, C., Pépin, L., Ritz, C., Saltzman, E., and Stievenard, M.: Climate and atmospheric history of the past 420,000 years from the Vostok ice core, Antarctica, *Nature*, 399, 429–413, <https://doi.org/10.1038/20859>, 1999.
- Ritz, S. P., Stocker, T. F., and Severinghaus, J. P.: Noble gases as proxies of mean ocean temperature: Sensitivity studies using a climate model of reduced complexity, *Quaternary Science Reviews*, 30, 3728–3741, <https://doi.org/10.1016/j.quascirev.2011.09.021>, 2011.
- 35 Rommelaere, V., Arnaud, L., and Barnola, J.-M.: Reconstructing recent atmospheric trace gas concentrations from polar firn and bubbly ice data by inverse methods, *Journal of Geophysical Research*, 102, 30 069–30 083, 1997.

- Sapart, C. J., Martinerie, P., Witrant, E., Chappellaz, J., Van De Wal, R. S., Sperlich, P., Van Der Veen, C., Bernard, S., Sturges, W. T., Blunier, T., Schwander, J., Etheridge, D., and Röckmann, T.: Can the carbon isotopic composition of methane be reconstructed from multi-site firn air measurements?, *Atmospheric Chemistry and Physics*, 13, 6993–7005, <https://doi.org/10.5194/acp-13-6993-2013>, 2013.
- Schwander, J.: The transformation of snow to ice and the occlusion of gases, *The Environmental Record in Glaciers and Ice Sheets H. Oeschger, CC Langway*, 53–67, 1989.
- Schwander, J., Stauffer, B., and Sigg, A.: Air mixing in firn and the age of the air at pore close-off, *Annals of Glaciology*, 10, 141–145, 1988.
- Schwander, J., Barnola, J.-M., Andrié, C., Leuenberger, M., Ludin, A., Raynaud, D., and Stauffer, B.: The age of the air in the firn and the ice at Summit, Greenland, *Journal of Geophysical Research*, 98, 2831–2838, <https://doi.org/10.1029/92JD02383>, 1993.
- Severinghaus, J. P. and Battle, M. O.: Fractionation of gases in polar ice during bubble close-off: New constraints from firn air Ne, Kr and Xe observations, *Earth and Planetary Science Letters*, 244, 474–500, <https://doi.org/10.1016/j.epsl.2006.01.032>, 2006.
- Severinghaus, J. P., Grachev, A., and Battle, M.: Thermal fractionation of air in polar firn by seasonal temperature gradients, *Geochemistry, Geophysics, Geosystems*, 2, 1–24, <https://doi.org/10.1029/2000GC000146>, 2001.
- Severinghaus, J. P., Albert, M. R., Courville, Z. R., Fahnestock, M. A., Kawamura, K., Montzka, S. A., Mühle, J., Scambos, T. A., Shields, E., Shuman, C. A., Suwa, M., Tans, P., and Weiss, R. F.: Deep air convection in the firn at a zero-accumulation site, central Antarctica, *Earth and Planetary Science Letters*, 293, 359–367, <https://doi.org/10.1016/j.epsl.2010.03.003>, 2010.
- Sowers, T., Bender, M., and Raynaud, D.: Elemental and Isotopic Composition of Occluded O₂ and N₂ in Polar Ice, *Journal of Geophysical Research*, 94, 5137–5150, <https://doi.org/10.1029/JD094iD04p05137>, 1989.
- Trudinger, C. M., Enting, I. G., Etheridge, D. M., Francey, R. J., Levchenko, V. A., Steele, L. P., Raynaud, D., and Arnaud, L.: Modeling air movement and bubble trapping in firn, *Journal of Geophysical Research: Atmospheres*, 102, 6747–6763, <https://doi.org/10.1029/96JD03382>, 1997.
- Trudinger, C. M., Etheridge, D. M., Rayner, P. J., Enting, I. G., Sturrock, G. A., and Langenfelds, R. L.: Reconstructing atmospheric histories from measurements of air composition in firn, *Journal of Geophysical Research Atmospheres*, 107, 1–13, <https://doi.org/10.1029/2002JD002545>, 2002.
- Trudinger, C. M., Enting, I. G., Rayner, P. J., Etheridge, D. M., Buizert, C., Rubino, M., Krummel, P. B., and Blunier, T.: How well do different tracers constrain the firn diffusivity profile?, *Atmospheric Chemistry and Physics*, 13, 1485–1510, <https://doi.org/10.5194/acp-13-1485-2013>, 2013.
- Van Ommen, T. D., Morgan, V. I., Jacka, T. H., Woon, S., and Elcheikh, A.: Near-surface temperatures in the Dome Summit South (Law Dome, East Antarctica) borehole, *Annals of Glaciology*, 29, 141–144, <https://doi.org/doi:10.3189/172756499781821382>, 1999.
- WAIS Divide Project Members: Precise inter-polar phasing of abrupt climate change during the last ice age, *Nature*, 520, 661–665, <https://doi.org/10.1038/nature14401>, 2015.
- Weller, G. and Schwerdtfeger, P.: Thermal properties and heat transfer processes of low-temperature snow, in: *Meteorological Studies at Plateau Station, Antarctica*, edited by Dalrymple, P. C., Riordan, A. J., Riordan, A., Riordan, A. J., and Weller, H. H. Lettau, H. Lettau, L. A. Stroschein, L. S. Kundla, Leander A. Stroschein, M. Kuhn, Peter Schwerdtfeger, R. C. L. a. R., vol. 25, American Geophysical Union, 1977.

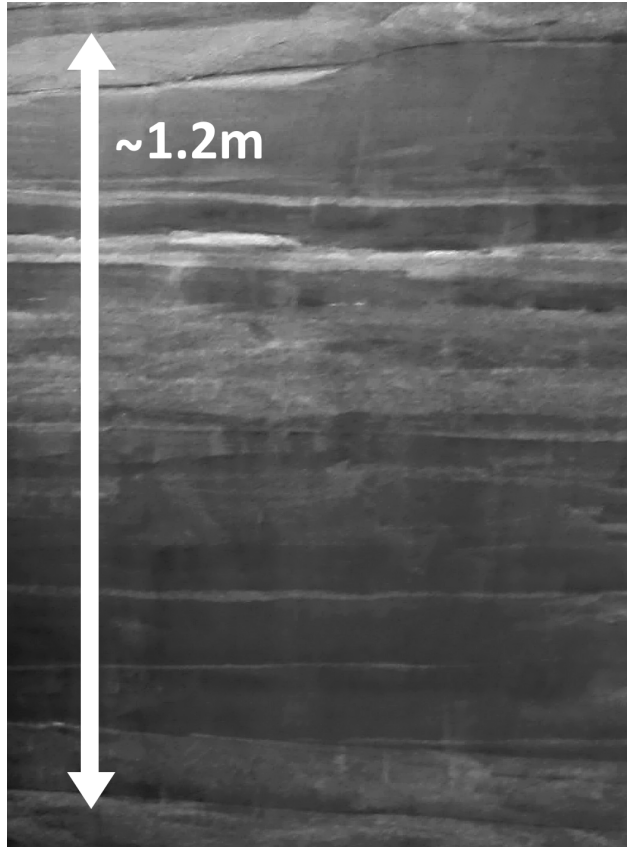


Figure 1. Layering of firn photographed in a surface pit at WAIS Divide. Image courtesy of Anaïs Orsi.

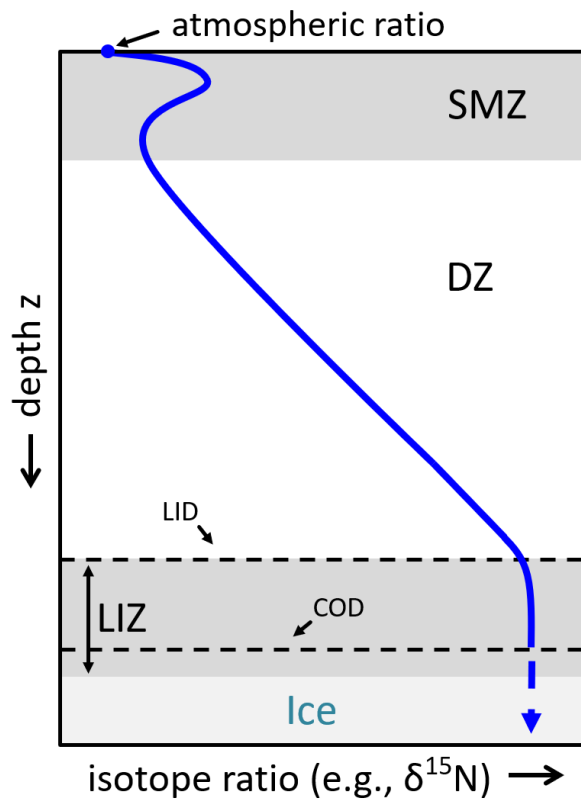


Figure 2. Schematic depiction of a typical isotope profile. The surface mixed zone (SMZ), the diffusive zone (DZ), the lock-in zone (LIZ) and the ice below are indicated by shading. Further indicated are the lock-in depth (LID) and the close-off depth (COD) (see text).

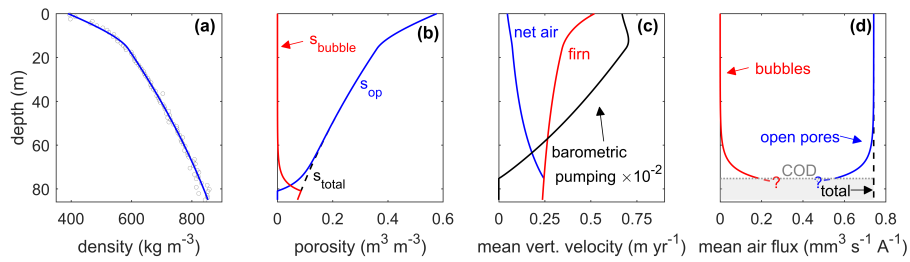


Figure 3. Firn conditions and modeled velocities profiles at WAIS Divide. (a) Density fit to observed data (data from Battle et al., 2011); (b) open, bubble (i.e., closed) and total porosity; (c) horizontally averaged barometric pumping velocity (i.e., time-mean horizontal average of $|\mathbf{u}_b|$, black), and horizontally averaged net air velocity ($\mathbf{w}_{firn} + \mathbf{w}_r$, blue) and firn velocity (\mathbf{w}_{firn} , red); (d) mean air flux in open pores (blue) and bubbles (red).

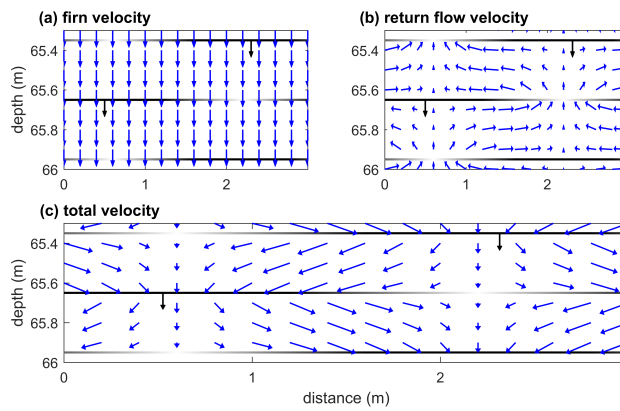


Figure 4. The different components of the velocity field. (a) firn velocity; (b) the velocity of air return flow to the atmosphere due to pore compression; (c) net firn air advection velocity (a linear combination of the fields in panels a and b). Because of its alternating direction, barometric pumping yields no net flow but instantaneous flow field patterns look similar to panel (b). Black arrows indicate the downward advection of layers at the firn velocity.

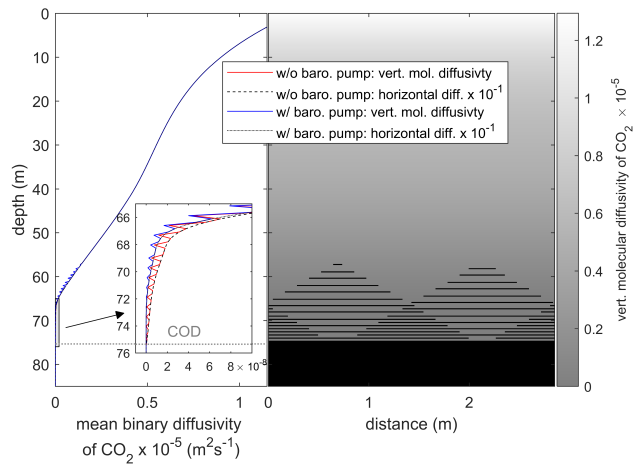


Figure 5. The CO₂ diffusivity profile at WAIS Divide. Left panel: Horizontally averaged, vertical and horizontal diffusivity in the model with and without barometric pumping. Right panel: map of diffusivity in the 2D model without barometric pumping. Only every third layer present in the model is shown here for clarity.

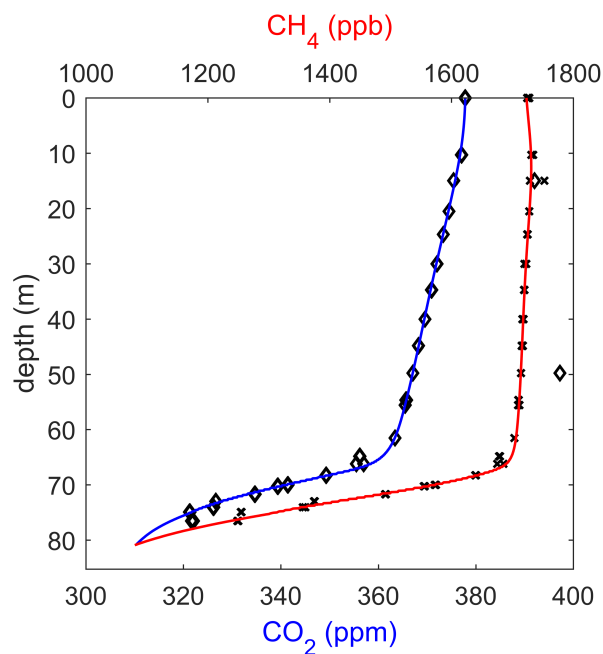


Figure 6. Simulated and observed CO₂ and CH₄ concentrations in the firn at WAIS Divide. The model is initialized with the recorded atmospheric trace gas concentrations in 1800 CE at all depths and is forced at the surface with histories of atmospheric CO₂ and CH₄ concentrations (Etheridge et al., 1996, 1998; Keeling et al., 2001; Buizert et al., 2012; Dlugokencky et al., 2016a, b). Markers indicate observed CO₂ (diamonds) and CH₄ (crosses) concentrations (Battle et al., 2011). Based on high CO₂ and CH₄, two samples at ~15 m and ~50 m depth were likely compromised by modern air during analysis and are thus ignored in the curve fit. Differences in the CO₂ and CH₄ profiles between the 1D model and the 2D model with or without barometric pumping are not visible at the resolution of this figure but are illustrated in the SI (Fig. S12).

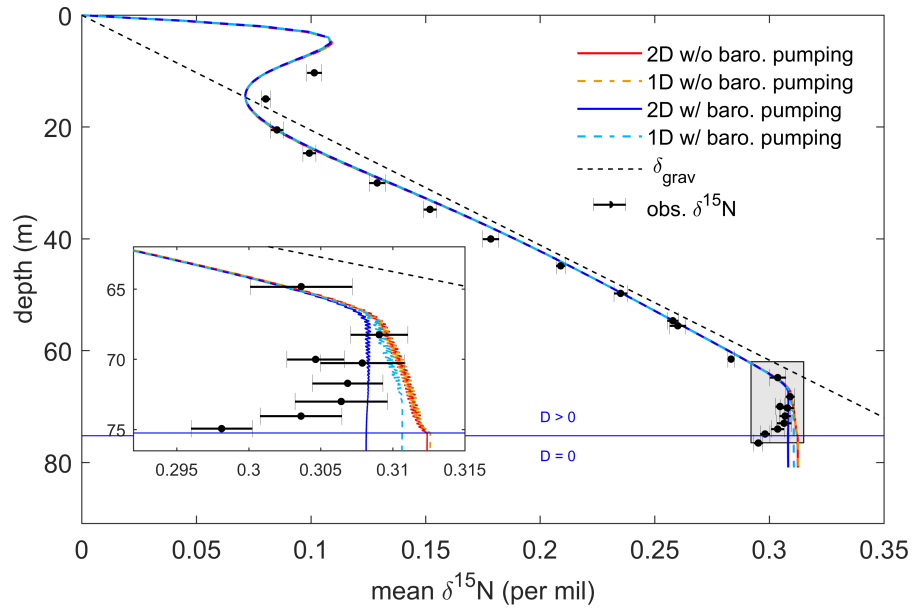


Figure 7. Horizontally averaged $\delta^{15}\text{N}$ at WAIS Divide. Model output is shown from four different versions of the 2D model (see text). Black circles with error bars indicate the observed firn $\delta^{15}\text{N}$ (Battle et al., 2011). The dashed black line represents the equilibrium solution for pure gravitational settling (δ_{grav}). The horizontal blue line marks the depth where vertical diffusivity reaches zero. The inset shows a magnification of the lock-in zone.

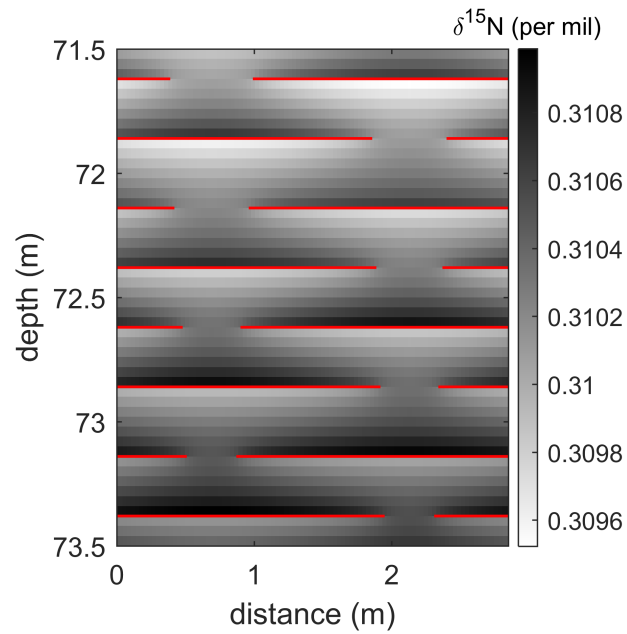


Figure 8. Simulated $\delta^{15}\text{N}$ in a part of the lock-in zone at WAIS Divide from the 2D model not including barometric pumping. Impermeable horizontal layers are shown in red. The size of the openings in the layers shrink with increasing depth.

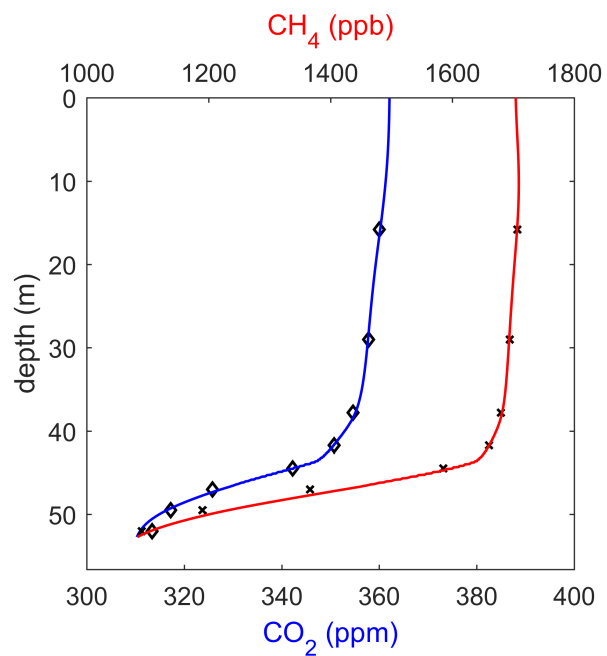


Figure 9. Simulated CO₂ and CH₄ concentrations in the firn at Law Dome DSSW20K. The model is forced with histories of atmospheric CO₂ and CH₄ concentrations from 1800 to 1998 CE (the date of sampling). Markers indicate observed CO₂ (diamonds) and CH₄ (crosses) concentrations (Trudinger et al., 2002).

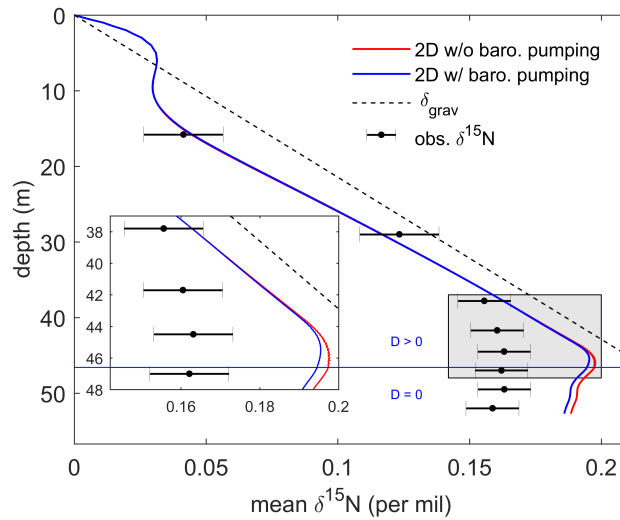


Figure 10. Horizontally averaged $\delta^{15}\text{N}$ at Law Dome DSSW20K. The solid lines show the results of the 2D model (with layers), for the cases with (blue) and without (red) barometric pumping. Black circles with error bars indicate the observed firm $\delta^{15}\text{N}$ (Trudinger et al., 2002, 2013). The dashed black line represents the equilibrium solution for pure gravitational settling (δ_{grav}). The horizontal blue line marks the depth where vertical diffusivity reaches zero. The inset shows a magnification of the lock-in zone.

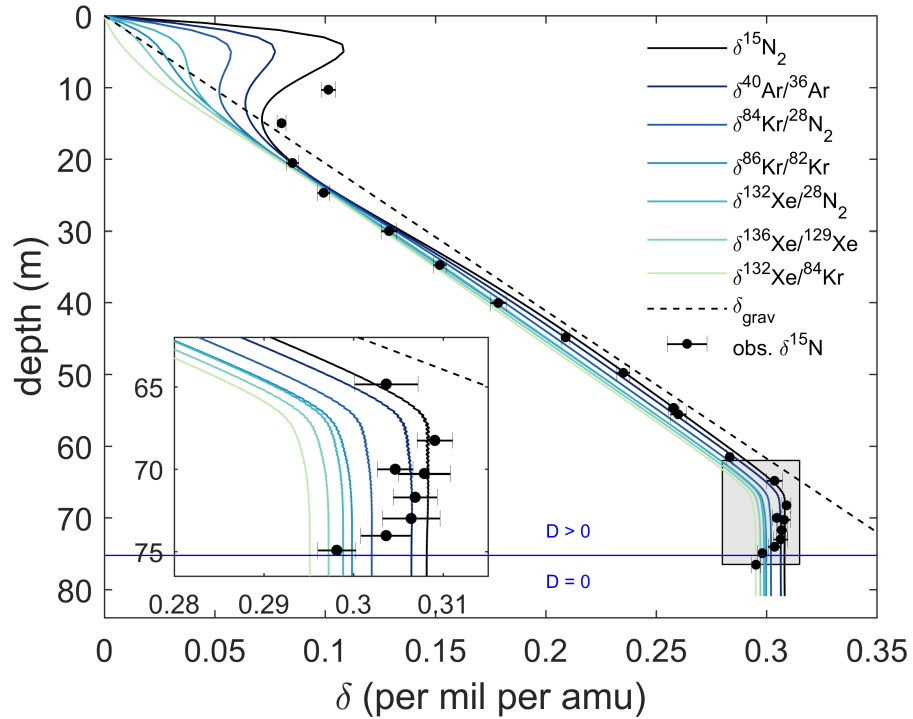


Figure 11. Horizontally averaged isotope ratios at WAIS Divide in the 2D model including barometric pumping and horizontal layers. Isotope ratios are normalized to one atomic mass unit (amu) mass difference (SI). The dashed black line represents the equilibrium solution for pure gravitational settling (δ_{grav}). The horizontal blue line marks the depth where vertical diffusivity reaches zero. Observed $\delta^{15}\text{N}$ are shown as circles with horizontal error bars (Battle et al., 2011). The inset shows a magnification of the lock-in zone (gray patch).

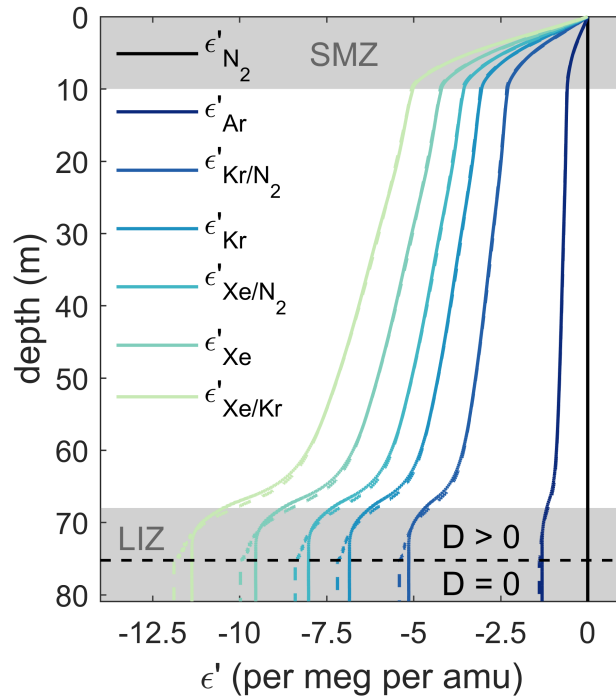


Figure 12. Differential kinetic isotope fractionation (ϵ') profiles for different isotope pairs at WAIS Divide. Colored solid and dashed lines show results from the 2D model with and without barometric pumping, respectively. ϵ' is defined as the (typically negative) difference between any mass-normalized isotope ratio and $\delta^{15}\text{N}$ (see text). Subscripts of one or two element names identify ratios as isotope or elemental ratios, respectively. The dashed black line highlights where molecular diffusivity in the model reaches zero.

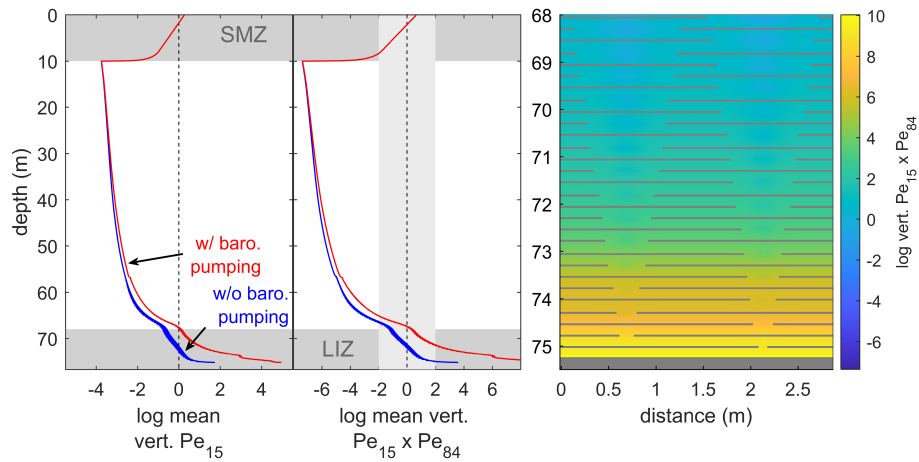


Figure 13. The balance of fractionating and non-fractionating mixing at WAIS Divide. The left panel illustrates the horizontally averaged modified Péclet number of $\delta^{15}\text{N}$ (Pe_{15} , see text). Blue and red lines show results from the 2D models with and without barometric pumping. The strength of dispersive mixing in the calculations is given by the mean barometric pumping flow velocities at the site. The middle panel displays the product of the modified Péclet numbers for $\delta^{15}\text{N}$ and $^{84}\text{Kr}/^{28}\text{N}_2$ (Pe_{84}). The region where ϵ' changes with depth should be greatest (i.e., where the product of the modified Péclet numbers is near one) is highlighted by a gray bar. The right panel provides a magnified 2D map of this Péclet number product in the LIZ.

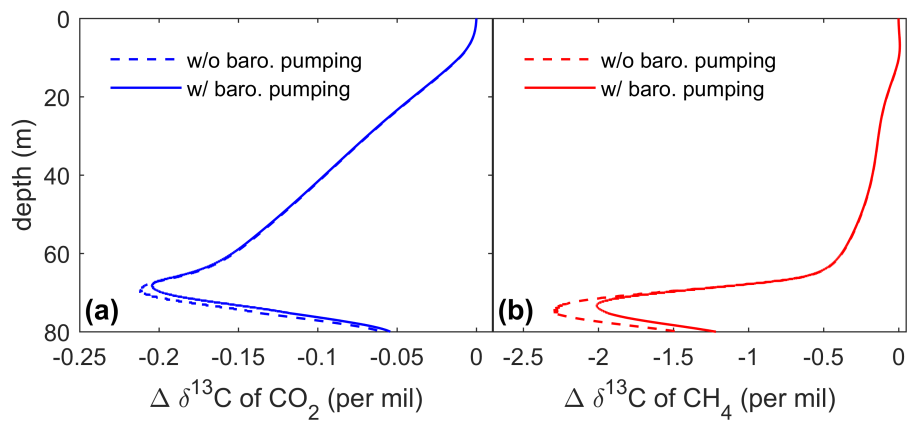


Figure 14. Diffusive fractionation effect at the time of sampling at WAIS Divide on $\delta^{13}\text{C}$ of (a) CO_2 and (b) CH_4 . Atmospheric mixing ratios of $^{12}\text{CO}_2$, $^{13}\text{CO}_2$, $^{12}\text{CH}_4$ and $^{13}\text{CH}_4$ were obtained from atmospheric trace gas histories used to drive the firm air model (see SI) and assuming constant atmospheric isotope ratios of -8‰ and -47‰ for $\delta^{13}\text{C}\text{-CO}_2$ and $\delta^{13}\text{C}\text{-CH}_4$, respectively. Firm air values are presented as the difference from the constant atmospheric isotope ratios.

Table 1. ϵ' scaling factor in the 2D model with barometric pumping between different element and isotope ratios from linear regression of ϵ' value pairs at all depths. $R^2 > 0.996$ for all relationships.

Predictor: isotope ratio	Response: time-variable atmospheric gas ratios		
	ϵ'_{Kr/N_2}	$\epsilon'_{Xe/Kr}$	ϵ'_{Xe/N_2}
ϵ'_{Ar}	3.94	8.74	6.16
ϵ'_{Kr}	0.75	1.66	1.17
ϵ'_{Xe}	0.54	1.19	0.84